




Article

Traffic Noise Mitigation Using Single and Double Barrier Caps of Different Shapes for an Extended Frequency Range

Domingo Pardo-Quiles , José-Víctor Rodríguez * , Jose-Maria Molina-García-Pardo and Leandro Juan-Llácer 

Departamento de Tecnologías de la Información y las Comunicaciones, Universidad Politécnica de Cartagena, Antiguo Cuartel de Antigonos, Plaza del Hospital, 1, 30202 Cartagena, Murcia, Spain;

domingo.pardo@upct.es (D.P.-Q.); josemaria.molina@upct.es (J.-M.M.G.-P.); leandro.juan@upct.es (L.J.-L.)

* Correspondence: jvictor.rodriguez@upct.es; Tel.: +34-968326548

Received: 9 July 2020; Accepted: 17 August 2020; Published: 19 August 2020



Abstract: The primary function of noise barriers is to shield inhabitants of affected areas from excessive noise generated by road traffic. To enhance the performance of noise barriers while simultaneously adhering to height restrictions, the attachment of structures (caps) of different shapes to the tops of conventional screens can be considered. These caps can significantly impact the diffracted sound energy, thereby increasing the desired global acoustic losses. This work presents a comprehensive study of the acoustic performance of noise barriers with single and double attached caps of different shapes through a calculation of their insertion losses (IL). This study comprehensively addresses and compares different types, sizes, combinations, and numbers of noise barrier caps for different scenarios (including sloping and absorbent grounds) and sources (“car” and “ambulance”) for an extended frequency band up to 10 kHz. To the best of the authors’ knowledge, this is a range that has not previously been analyzed. A variety of different cap shapes were considered including cylinders, rectangles, trapezoids, and Y/T-shaped forms. To calculate the IL , an innovative and fast uniform theory of diffraction (UTD)-based method developed by the authors was applied in all simulations. The results showed that the Y-shaped single and double barrier caps were, in general, the most effective at increasing IL without raising the height of the barrier, thereby successfully managing the aesthetic impact. The results also showed how the consideration of sloping and absorbent floors could also contribute to improved noise abatement.

Keywords: traffic noise mitigation; noise barriers; noise barrier caps; sound attenuation; uniform theory of diffraction

1. Introduction

The World Health Organization’s report on night-noise guidelines for Europe and the burden of disease from environmental noise affirms that about 20% of the European population is exposed to road traffic noise at levels exceeding 65 dBA (equivalent sound pressure level [SPL] with A-frequency weighting) [1]. This noise level is higher than the maximum acceptable outdoor value in living environments in many European countries [2]. The perception of noise as annoying depends primarily on noise levels and the source producing such noise [3]. Noise can affect human health [4], cause sleep disorders [5], annoyance [6], learning impairment [7,8], hypertension ischemic heart disease [9,10], diabetes risk [11], and loss of hearing [12]. This is why there is an urgent need to control noise pollution, especially in sensitive areas such as near hospitals and schools.

Traditionally, the most common method for traffic noise abatement has been noise barriers, which can significantly reduce the noise exposure of a single receiver. There is growing interest in

low-noise pavements to reduce traffic noise because the benefits of silent pavements are enjoyed by many receivers. Road pavement is a principal factor in traffic noise. Parameters such as texture [13] and granulometry properties [14] are very important when assessing superficial properties, and these cannot be disregarded in the evaluation of pavement quality [15–17]. Sonic crystal barriers are a more recent development. These are a modern and sustainable solution for traffic noise mitigation, but the technology still needs further development [18–20].

Noise barriers can be formed using earth mounds (“berms”) positioned along roads, high walls, or a combination of both. These barriers do not eliminate traffic noise, but they reduce it substantially, improving the quality of life of people who live adjacent to busy roads. However, different structures (caps) attached to the tops of the barriers can enhance their noise isolation performance with a barely perceptible increase in the height of the original barrier (depending on the shape of the structure). Caps thus improve noise mitigation and maintain existing aesthetics, and can be incorporated during the initial design phase or by retrofitting existing barriers. It is important to note that, given that walls are subject to maximum height restrictions, simply increasing a wall’s height to avoid the need for a cap is not always an appropriate solution for noise attenuation.

The existing literature has examined the performance of various caps. For example, Watts [21–24], Haan [25], Ishizuka [26], Asdrubali [27], and Monazzam [28] considered different diffracting structures (e.g., multiple-edge, T-profile, and cylindrical caps). The Japanese experience of reducing road traffic noise from the 1990s to 2000s is also relevant, as this period saw several commercial developments of edge-modified barriers [29]. Nevertheless, since then, research into this area has progressively decreased because the tested models (e.g., modified cylinders, T-shaped, Y-shaped, and mushroom-type) have failed to achieve the expected noise reduction efficiencies [30].

According to the Quietness and Economics Stimulate Infrastructure Management (QUESTIM) noise barrier survey [31], which was later confirmed by [32], the aforementioned cap elements are largely unused across Europe because of the lack of noise-modeling software, the lack of data confirming their effectiveness, and cost reasons. The above authors [21–28] typically analyzed single or multi edge-modified devices, but without systematically checking possible combinations of such structures and/or without extending the frequency range of evaluation further than 4–5 kHz.

Therefore, in this work, an extensive and comprehensive study of the acoustic performance of differently shaped single and double reflective structures (cap elements) attached to the top of conventional noise barriers was carried out by calculating their sound pressure *insertion losses* (*IL*). Acoustic *IL* is a parameter commonly used to evaluate and compare the performance of different noise barriers, so this parameter will be considered. To calculate the *IL* in this study, an innovative, fast uniform theory of diffraction (UTD)-based method developed by the authors was applied in all simulations. The cap shapes chosen for analysis covered a wide range of structures including cylinders, rectangles, trapezoids, and Y/T-shaped structures. All of these shapes were properly standardized with equivalent dimensions and/or envelopes to ensure that reliable comparisons could be made. Moreover, four different configurations (with two transmitter and receiver positions) were considered. It should be noted that the use of absorptive materials on barrier caps would further enhance the barriers’ *IL* performance; however, real-life testing of certain barrier caps (e.g., T-profile caps) has not revealed a significant difference between the *IL* performance of absorptive and reflective configurations [33]. Therefore, absorptive cap materials were not considered in the present work. Finally, the influence on *IL* of the ground reflection of the acoustic wave on the barrier side closer to the receiver and transmitter is also discussed (unless otherwise specified, ground reflections are always considered in the results presented in this study).

The novelty and main contribution of this study lie in the fact that it comprehensively addresses and compares different types, sizes, combinations, and numbers of noise barrier caps for different scenarios (including sloping and absorbent grounds) and sources (“car” and “ambulance”) for an extended frequency band up to 10 kHz. To the best of the authors’ knowledge, a study like this has not been previously published. Moreover, all cases have been studied with a frequency resolution higher

than 3000 frequency bins. In this regard, it should be mentioned that this task has been carried out with quite low computational effort thanks to the speed of the UTD-based approach developed by the authors; the same extensive and painstaking analysis would have been extremely time-consuming with other approaches such as the boundary element method (BEM).

2. Materials and Methods

2.1. Traffic Noise Spectrum

The spectrum of traffic noise can be influenced by a variety of factors including flow rate, type, and speed of vehicles, road surface, and weather conditions. There is a huge body of work examining the spectra of road traffic noise sound pressure level (SPL) recorded in many countries taking into account the aforementioned factors [34–36]. In most of these studies, significant low-frequency SPL content has been identified for vehicle speeds lower than 50–60 km/h (31–37 mph) caused by the vehicles' engine and transmission and the interaction of the tires with the road surface. Spectra peaks commonly shift to higher frequencies when the vehicle speed increases. Nevertheless, traffic noise spectra levels usually decrease in magnitude at frequencies higher than 1 kHz. The one-third octave band normalized spectra of noise source for A-weighted road traffic noise given in the European Standard EN1793-3:199719 [37] is widely used in Europe as a reference. For the present work, the road traffic spectrum source was taken from [38], which in turn was based on the cited standard and is shown in Figure 1.

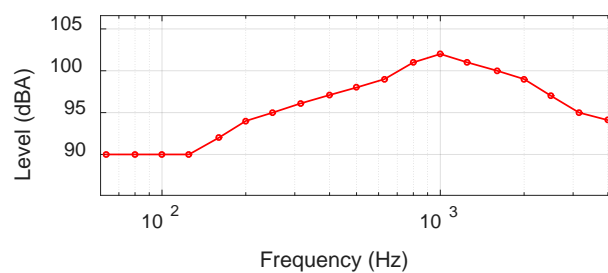


Figure 1. A-weighted sound power level (L_w) spectrum. Road traffic noise spectrum according to [38].

Due to the decrease, at a certain point, of the curve depicted in Figure 1, IL is typically studied in relation to frequencies lower than 3 or 4 kHz. However, there is another relatively common source of noise that needs to be considered, specifically, emergency sirens (e.g., ambulance, police car, etc.), which feature a higher frequency content, as reported by Catchpole [39] and Howard [40].

The radiated acoustic power is a recommendable method to characterize these types of sound sources, as it is independent of the measurement distance and mounting location of the siren. An example of siren noise recorded by Howard [40], which has been chosen for the present work, is shown in Figure 2.

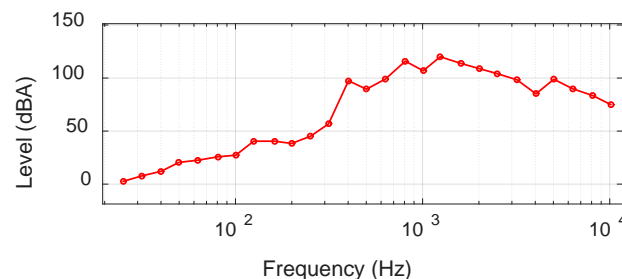


Figure 2. A-weighted sound power level (L_w) spectrum of a typical siren by Howard [40].

The sound power levels (A-weighted) of the siren selected were the “UK fire brigade” type (Figure 2). In any case, the results of the one third octave band sound power measurements in [40] showed that

all sirens exhibited similar sound power levels for the same frequency range including the French or Italian ambulance sirens presented by Howard. Therefore, the election of any other siren for this work would have been practically inconsequential, providing similar results.

As can be observed, the spectral content of typical sirens reach frequencies close to 10 kHz. Therefore, in this work, unlike in previous studies, an extended frequency range of up to 10 kHz was assumed, along with an additional specific scenario in which an ambulance siren sound source was located at a typical height of 2.5 m, as described in the following section.

2.2. Propagation Environment

The four propagation schemes considered in this work are illustrated in Figures 3 and 4. These schemes consist of:

- Noise sources (T_{x1} and T_{x2} , respectively) that radiate sound spherically at a height (h_{tx1}) of 0.5 m (location C for “car”) with the SPL spectrum displayed in Figure 1, or from a vehicle with a light-bar mounted siren at a height (h_{tx2}) of 2.5 m (location A for “ambulance”) with the SPL spectrum displayed in Figure 2.
- Barrier located at a distance (d_1) of 3 m from the sound source and a height (h_{bar}) of 3 m with a maximum width (w) of 0.4 m (including their single or double cap on the top).
- Potential sound receivers (R_{x1} and R_{x2}) positioned at a distance (d_2) of 7 m from the barrier at heights of $h_{rx1} = 1.7$ m (location P for “person”) and $h_{rx2} = 5$ m (location B for “balcony”), respectively.

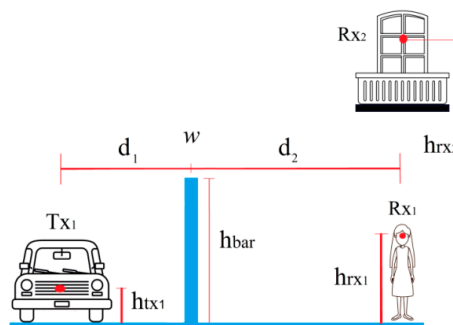


Figure 3. Car configurations (‘1’, person, and ‘2’, balcony).

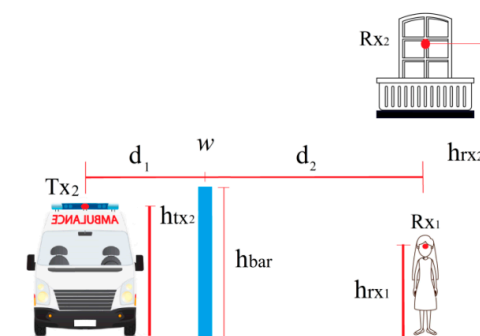


Figure 4. Siren vehicle configurations (‘3’, person and ‘4’, balcony).

Therefore, the four schemes are as follows:

- Configuration 1 (C–P), ‘Car–Person’.
- Configuration 2 (C–B), ‘Car–Balcony’.
- Configuration 3 (A–P), ‘Ambulance–Person’.
- Configuration 4 (A–B), ‘Ambulance–Balcony’.

It should be noted that to properly analyze the performance of the acoustic barriers, they must be tall enough to block the line-of-sight (LoS) from the road to the receiver. This can be achieved with a barrier of a relatively low height when the ground profile is not steeply sloped, the receiver is a person on the ground, and/or the acoustic barrier is close to the hard shoulder of the road (where the noise source is located). It should be explained here that the LoS arises between the source and the listener in the Ambulance–Balcony configuration and should thus be considered when testing the effect of the attached caps in this scenario.

In the U.S., the average noise barrier heights vary widely from 2.1 m to up to approximately 5.5 m [41]. Across Europe, the minimum permissible height ranges from 1.0 m to 2.5 m, but the maximum permissible heights can vary from 4 m to 10 m or even higher, making the overall variations in barrier height seen in Europe far more significant than that seen in the U.S. [31]. Given the above, a moderate barrier height of 3 m was applied in the simulations of the present work. There are several reasons for this choice: it is cost-effective in terms of the investment required to build barriers of this height; it results in an aesthetic benefit for the surroundings; this height falls well within the average permitted noise barrier heights in both Europe and the U.S.; and it is a common height applied in studies undertaken in Japan (e.g., Morgan [42]).

For each of the four propagation configurations analyzed, five reflective barrier cap models were considered. The cross-sections of each cap model are illustrated in Figure 5.

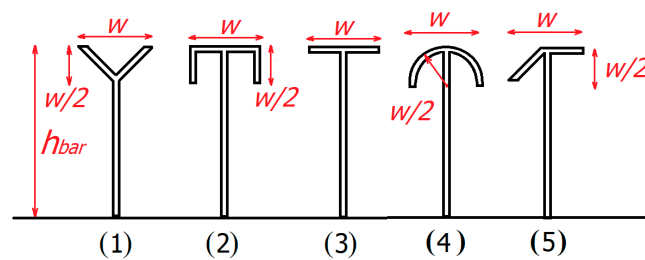


Figure 5. Barrier caps considered: (1) Y-shaped; (2) rectangular; (3) T-shaped; (4) cylinder with radius $w/2$; and (5) trapezoid-shaped.

Additionally, further analysis of the configurations illustrated in Figures 3 and 4 was conducted with barrier arrangements formed by two caps combined and resized to adhere to the maximum structure envelope size (total width of w and a height of $w/2$) and leaving a free space between them of $w/4$, as shown in Figure 6.

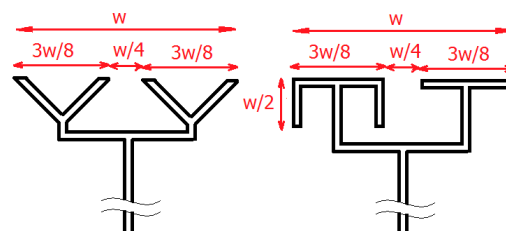


Figure 6. Examples of double-cap barriers of all possible existing combinations. The total envelope size is maintained.

There are 25 possible structural combinations of double-cap barriers (5^2). It should be noted that the internal reflections between barrier caps over the mid support structure were intentionally not considered as their influence on the final pressure level is negligible.

Therefore, a total of 100 simulations for the 25 double-cap barrier combinations and the four configurations of sources and receivers, plus 20 simulations for all single-noise barrier scenarios, besides four simulations for single screen barriers (as a base reference), were conducted, meaning

that a total of 124 simulations were undertaken in the frequency range of 100 Hz to 10 kHz. Each simulation with one scenario and combination of caps implies calculating the global complex sound pressure field at the receiver from all possible paths per each frequency point (e.g., 3000 frequency bins). Finally, the influence of the slope of the ground on the global acoustic *IL* as well as the consideration of triple caps is briefly discussed.

2.3. Theoretical Method

The method implemented is based on an innovative two-dimensional (2-D or 2.5 D, if we take the ground reflection into consideration) formulation founded in UTD (uniform theory of diffraction) to analyze multiple diffraction/reflection of acoustic waves; the authors demonstrated, made comparisons, and validated such formulation in [43]. The implemented model is deterministic (it does not pose any inherent randomness), for which the output is fully determined by the parameter values and the initial conditions. This UTD methodology is enhanced by using graph theory, Fresnel ellipsoids, and funicular polygons, so that consideration is only given to those paths and obstacles in this complex environment that make a contribution to global *IL*. This allows for the provision of swift, accurate, and efficiently computed predictions for sound attenuation, something that cannot be achieved by employing alternative more time demanding techniques (e.g., BEM). Using this technique, a substantial quantity of obstacles (which includes adjacent ones of the same height) may be managed in high-frequency resolution and in a sufficiently short time. We can model the obstacles as cylinders, rectangles, wedges, or knife edges, and also as a number of other polygonal deflecting obstacles (e.g., T- or Y-shaped barriers or trapezoids).

In this manner, the total diffracted (and reflected on ground/floor) complex pressure field emanating from a source *Tx* at any frequency to the receiver *Rx* will represent the entirety of the rays converging on *Rx* on every possible path:

$$\phi_{tRx} = \sum_{i=1}^n \phi_{t_{path\ i}}(Tx, Rx), \tag{1}$$

with $\phi_{t_{path\ i}}(Tx, Rx)$ being the complex received field for one ray from *Tx* to *Rx*, which follows one possible selected path *n*. It is assumed that *Tx* is a point source generating spherical wave fronts in the context of a perfect isotropic (uniform) medium (e.g., air), whilst the receiver of this acoustic field *Rx* is a listener where the isotropic pattern has unity gain. Consideration of the phase occurs for every signal on every path, utilizing the UTD theory combining the diffraction phenomenon with ray representation, permitting the field at the receiver to be calculated as a vector derived from combining all the fields that correspond with each ray.

Every frequency bin is then run on a loop from the minimum to maximum to derive the whole sound pressure field for a full set of paths on a specific frequency. With every frequency, the algorithm further permits checking of the sound pressure field levels for every path at the receiver. With sorting of the set of paths, it is predicted that the derived sub-fields will progressively decrease, defining an adjustable pressure condition that can block new fields from being added when the current field does not meet the threshold. We may define the threshold as being the absolute value for the ratio between the signal level received on the shortest path at this frequency and the signal level received for the current path (e.g., 1×10^{-5}). When the threshold level is set at 1, this ensures that no path is discarded. It is important to note that the compensation time for this suggested algorithm is independent of frequency and may be restrained or limited at any time, as worst-case scenarios can be predicted through the multiplication of consumed times at any frequency by the quantity of frequency bins under consideration in the simulation.

Regarding the above, obtaining the complex field at the receiver for all frequencies and all paths may be achieved using the following expression:

$$\phi_{t_{path\ i}} = \frac{\phi_0}{s_T} \cdot e^{-jks_T} \cdot \prod_{n=1}^{N-2} \left(\frac{D_n}{R_n} \right) \cdot \sqrt{\frac{s_T}{\prod_{i=1}^{N-1} (s_i)}} \cdot \gamma \cdot e^{-\alpha s_T} \tag{2}$$

where:

ϕ_0 represents the SPL from the source;

$s_T = \sum_{i=1}^N s_i$, with s_i representing the slant distances for the links of paths chosen, between each node's geometrical centers;

k represents the wavenumber;

N represents the quantity of nodes for every path;

D_n represents the diffraction coefficient and R_n the reflection coefficient; application is dependent on the form of incidence either obstacle or ground;

γ represents the obstacle coefficient factor. The expression is derived from [44,45], but includes, in this instance, the γ coefficient factor for two reasons: to adjust the phase, and to be a weight factor ([46,47]) for every form of obstacle under consideration in this research.

α is the air-absorbent coefficient in Np/m, according to [48]. In turn, this parameter depends on the following input variables, which are related to the source's frequency emission (f) and the physical properties of the air: static pressure (P_s), Celsius temperature (T), and percentage relative humidity (H).

PARDOS (acronym from Spanish 'Pérdidas Acústicas por Reflexión y Difracción de la Onda Sonora', which means 'Acoustic Losses due to Reflection and Diffraction of Sound Waves') is a user-friendly software tool developed ad-hoc with MATLAB in order to be used for the simulations conducted in this work. The authors demonstrated, made comparisons, and validated such a formulation in [43]. Figure 7 summarizes the flow chart of the software tool's core to obtain the sound pressure spectrum:

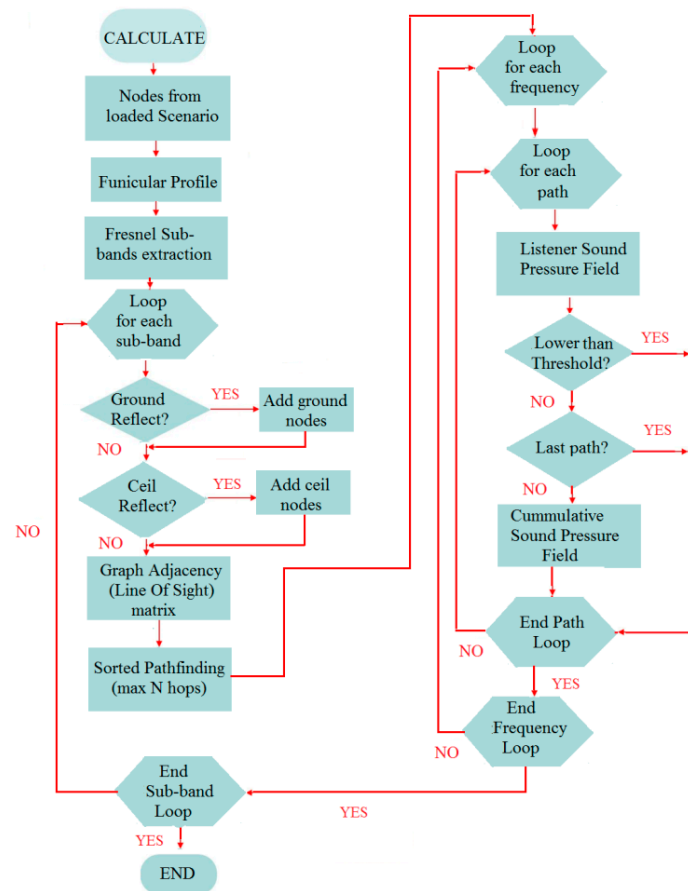


Figure 7. 'Calculate' subroutine flow diagram.

Figure 8 shows a general view of the PARDOS graphical user interface (GUI):

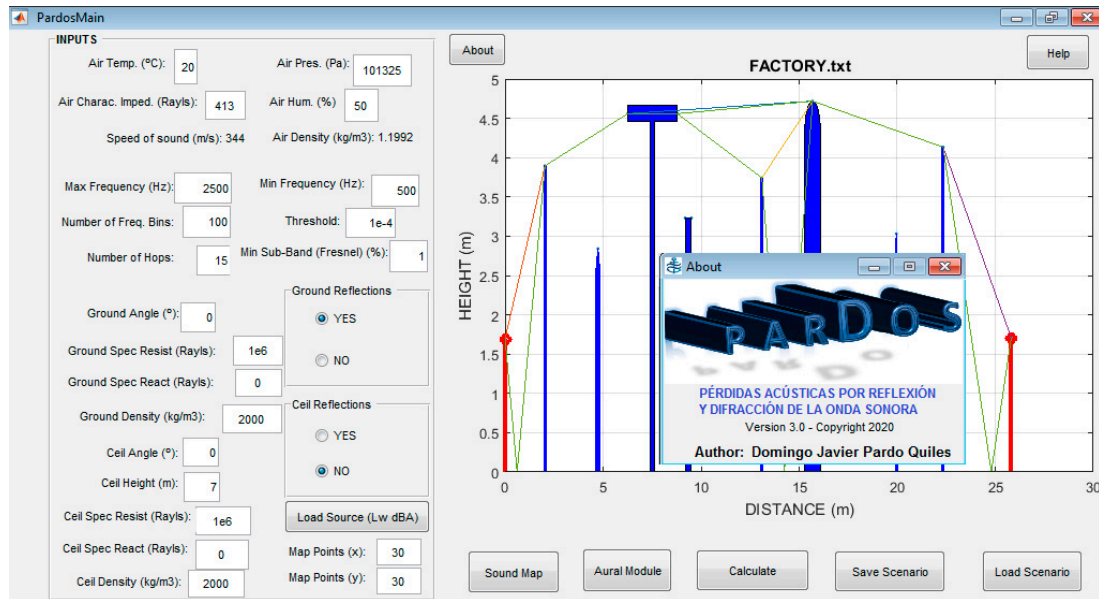


Figure 8. PARDOS (Pérdidas Acústicas por Reflexión y Difracción de la Onda Sonora) main GUI (graphical user interface) with ‘About’ pop-up window.

Two assumptions were made in the present algorithm and tool developed by the authors: first, the far field region was met (which is true for distances from the source clearly greater than a wavelength of sound); and second, no contribution through the barriers (acoustic isolation) was accounted for (which does not imply any constraint since it is intended to evaluate the performance of the diffracting structures). Therefore, these two approaches did not turn out to have any restrictions on the results obtained.

2.3.1. Pressure Diffraction Coefficients (Dn)

According to UTD [45], the pressure diffraction coefficient for knife-edges and wedges can be defined as:

$$D(v, k, L, s_1, s_2, \theta_2, \theta_1) = \frac{-e^{-i\frac{\pi}{4}}}{2v \sqrt{2\pi k}} \cdot \begin{bmatrix} \tan^{-1}\left(\frac{\pi+(\theta_2-\theta_1)}{2v}\right) \cdot F(kLa^+(\theta_2 - \theta_1, v)) \\ + \tan^{-1}\left(\frac{\pi-(\theta_2-\theta_1)}{2v}\right) \cdot F(kLa^-(\theta_2 - \theta_1, v)) \\ + R_n \cdot \tan^{-1}\left(\frac{\pi+(\theta_2+\theta_1)}{2v}\right) \cdot F(kLa^+(\theta_2 + \theta_1, v)) \\ + R_0 \cdot \tan^{-1}\left(\frac{\pi-(\theta_2+\theta_1)}{2v}\right) \cdot F(kLa^-(\theta_2 + \theta_1, v)) \end{bmatrix} \quad (3)$$

where R_0 and R_n represent the reflecting coefficients for adjacent (0) and opposite (n) obstacle faces seen by the incident wave. The reflecting coefficients R_0 and R_n will depend on: the incident (θ_1) and diffracting (θ_2) angles of the path between the source and receiver, respectively; and the normal specific acoustic impedances of the faces seen by them (Figure 9). Further explanations are provided in Section 2.3.2, and [45] offers greater detail regarding all these parameters:

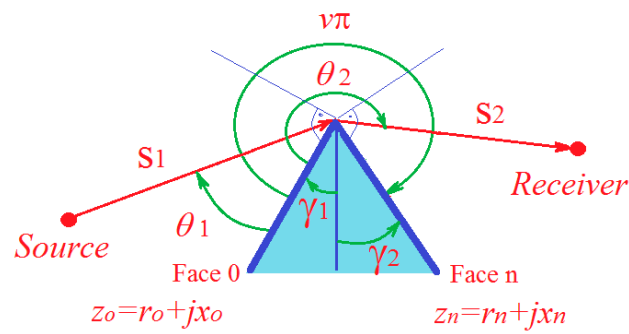


Figure 9. Notation used in a single diffracting wedge. Reflection coefficients for the 0 face, with incidence angle θ_1 , and for the n face, with reflection angle $v\pi - \theta_2$.

$F[x]$ represents the “transition function”, which can be defined as a Fresnel integral [45]:

$$F[x] = 2i \sqrt{x} e^{ix} \int_{\sqrt{x}}^{\infty} e^{-iu^2} du, \tag{4}$$

$$L = \frac{s_i s_j}{s_i + s_j} \tag{5}$$

and

$$a^\pm(\beta) = 2 \cos^2\left(\frac{2v\pi N^\pm - \beta}{2}\right), \beta = \theta_2 \pm \theta_1 \tag{6}$$

where N^\pm are the integers that most nearly satisfy the equations

$$2\pi v N^+ - \beta = \pi, \tag{7}$$

$$2\pi v N^- - \beta = -\pi. \tag{8}$$

In the same way, we may employ UTD to explain the diffraction coefficient with cylindrical structures using a pair of scattering mechanisms, either being the field’s diffraction or reflection components [49,50]. Thus with the “shadow region” (source-receiver line-of-sight (LoS) absent), we may consider this diffraction coefficient:

$$T_{s,h}(a) = -m_p \sqrt{\frac{2}{k}} e^{-i\frac{\pi}{4}} e^{-ikt(a)} \left\{ \frac{-F[X(a)]}{2\varepsilon(a) \sqrt{\pi}} + [q^*(\varepsilon(a))] \right\}, \tag{9}$$

being

$$a = \pi + \alpha + \beta, \quad \alpha, \beta \geq 0 \tag{10}$$

$$X(a) = \frac{kL(a - \pi)^2}{2}, \tag{11}$$

$$\varepsilon(a) = m_p(a - \pi), \tag{12}$$

$$m_p = \left(\frac{k \cdot r_{obs}}{2}\right)^{\frac{1}{3}}, \tag{13}$$

$$t(a) = (a - \pi)r_{obs}, \tag{14}$$

where α and β are the angles of the arc run by the ‘creeping’ wave over the rounded surface; k is the wavenumber; r_{obs} is the radii of the cylinder; and s_i and s_j are the slant ranges from the source and receiver, respectively.

A comprehensive description of each variable is explained in [49,50] as well as in [43]. The first addend of Equation (9) describes the Fresnel diffraction process. $F[x]$ represents the “transition function” already defined in Equation (4).

For the second extension of Equation (9), the term $q^*(\varepsilon(a))$ represents the “Fock scattering function”, which deals with ‘creeping’ waves generated along a smooth body’s surface (e.g., spheres or cylinders [49]).

In the same way, in the “lit region” (source/receiver line-of-sight), we may alternatively apply this diffraction coefficient:

$$R_{s,h}(a) = -\sqrt{\frac{r}{m_p}} e^{-i\frac{\varepsilon^3(a)}{12}} e^{-i\frac{\pi}{4}} \left\{ \frac{-F[X(a)]}{2\varepsilon(a)\sqrt{\pi}} + [q^*(\varepsilon(a))] \right\}, \tag{15}$$

where

$$\varepsilon(a) = -2m_p \left(\cos\left(\frac{a}{2}\right) \right), \tag{16}$$

$$X(a) = 2kL \left(\cos\left(\frac{a}{2}\right) \right)^2, \tag{17}$$

with L as in Equation (5), m_p as Equation (13), and a is the angle between the incident and the diffracted ray

$$a = \theta_2 - \theta_1, \tag{18}$$

The parameters are similarly further detailed in [49–51] and in [43].

2.3.2. Pressure Reflection Coefficients (R_n, R_o)

The method chosen for analyzing the Rayleigh reflection coefficient of waves obliquely incident on the surface of a solid (either on the ground, ceiling, or on any obstacle surface) with a known normal-specific acoustic impedance can be reviewed in Chapter 6 in [52]. Providing that the surface is acoustically smooth, without the irregularities of the order of a wavelength in size, sound wave-fronts will not be scattered in other directions and will be reflected as largely intact (Chapter 12 in [53]).

If the speed of sound in air (c_{air}) is higher than that of the solid media (c_{solid}), or if c_{air} is lower than that of the solid medium, but the angle of incidence θ_i is less than the critical angle θ_c ,

$$\theta_c = \text{asin}\left(\frac{c_{air}}{c_{solid}}\right), \tag{19}$$

then the Rayleigh reflection coefficient would be:

$$R = \frac{\frac{r_1}{z_o} - \frac{\cos(\theta_t)}{\cos(\theta_i)} + \frac{jx_1}{z_o}}{\frac{r_1}{z_o} + \frac{\cos(\theta_t)}{\cos(\theta_i)} + \frac{jx_1}{z_o}}, \tag{20}$$

with r_1 and x_1 being the resistance and reactance, respectively, of the complex normal-specific acoustic impedance of the solid material defined as:

$$z_1 = r_1 + jx_1, \tag{21}$$

with z_o being the characteristic impedance of the air, and

$$\cos(\theta_t) = \sqrt{1 - \left(\frac{c_{solid}}{c_{air}}\right)^2 \cdot \sin^2(\theta_i)} \tag{22}$$

where θ_t is the angle of transmission in the solid.

Otherwise, if $c_{solid} > c_{air}$ and under the restriction $\theta_i > \theta_c$, then the reflection coefficient would be:

$$R = e^{i\varnothing}, \tag{23}$$

with

$$\varnothing = 2 \cdot \text{atan} \left[\left(\frac{\rho_{air}}{\rho_{solid}} \right) \cdot \sqrt{\left(\frac{\cos(\theta_c)}{\cos(\theta_i)} \right)^2 - 1} \right], \tag{24}$$

and ρ_{air} and ρ_{solid} being the densities of the air and solid, respectively.

Finally, the total sound pressure at the receiver for each frequency bin will be the summation of all the sound pressure signals for all the selected paths arriving at the receiver, as shown in Equation (1). The last step is to estimate the *IL* at any frequency using the following equation:

$$IL \text{ (dB)} = 20 \cdot \log_{10} \left(\left| \frac{\phi_{fs}}{\phi_{tRx}} \right| \right), \tag{25}$$

where ϕ_{tRx} is the total sound pressure field at the receiver at each frequency considering obstacles and ϕ_{fs} is the sound pressure field at the receiver in free space (without considering obstacles). It should be noted that, in the absence of obstacles, the parameter ϕ_{fs} must also consider both the reflections on the ground and ceiling.

2.3.3. Global Sound Pressure Level Estimation

Once the 124 simulations were conducted with PARDOS and an optimum barrier cap (in terms of maximum *IL*) was identified for the four configurations considered, the global SPL in dBA at the receiver locations was calculated. This was achieved by considering the noise spectra of road traffic and typical siren sources (depicted in Figures 1 and 2, respectively) along with the optimum noise barrier previously identified. This calculation aims to assess whether the expected global values are below those recommended by the World Health Organization (WHO) [2] for the situations considered.

To carry out this assessment, the following steps were applied:

- Transformation of the A-weighted power level L_w (dBA) into the A-weighted SPL L_p (dBA) at 1 m:

$$L_p(\text{dB(A)}) = L_w(\text{dB(A)}) - \left| 10 \cdot \log_{10} \left(\frac{Q}{4\pi r^2} \right) \right|, \tag{26}$$

where Q is the directivity factor and r is the distance to the source.

The distance r to the sound source for which the sound pressure levels were calculated was 1 m for both types of sources ('car' and 'ambulance'). Spherical propagation (isotropic propagation) was also considered, for which Q must be equal to 1. Under these two assumptions, the sound pressure level (L_p) of a point source was 11 dB less than its sound power level (L_w) at any frequency.

- Normalization of the pressure level from one-third octave band spectra to 1 Hz frequency resolution with a linear distribution. A simple loop runs for all the center frequencies $f_{0,i}$ of each 1/3rd octave frequency band (Δfi). The sound pressure levels at the 1 Hz band resolution was obtained by normalizing each $L_p(\text{dB(A)})$ value by their correspondent frequency band Δfi , as shown in Equations (27) to (30):

$$\Delta fi = f_{2,i} - f_{1,i} = \sqrt[3]{2} f_{1,i} - f_{1,i}, \tag{27}$$

$$f_{0,i} = \sqrt{f_{1,i} \cdot f_{2,i}}, \tag{28}$$

$$\Delta fi = \left(\sqrt[6]{2} - \frac{1}{\sqrt[6]{2}} \right) \cdot f_{0,i} \approx 0.23156 \cdot f_{0,i}, \tag{29}$$

$$L_p(\text{dB(A)})_{1\text{Hz}} = L_p(\text{dB(A)}) - 10 \cdot \log_{10}(\Delta fi), \quad \forall f \in [f_{1,i} - f_{2,i}], \tag{30}$$

where $f_{1,i}$ and $f_{2,i}$ are the lower and upper cut-off frequencies of the 1/3rd octave band Δf_i , respectively. In this way, the sound pressure level is properly conserved as it is just distributed among each frequency band. The integration of the signal within each sub band would result in the former $L_p(\text{dB(A)})$ value. Figures 10 and 11 show the resulting transformation of the selected sources from Figures 1 and 2:

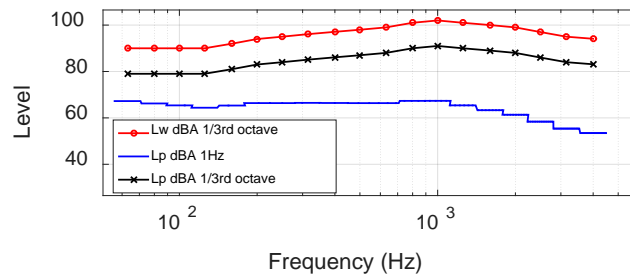


Figure 10. A-weighted sound power level (L_w), SPL (L_p dBA 1/3rd octave) equivalent spectra of road traffic noise at 1/3rd octave frequency band and 1 Hz resolution band (L_p dBA 1 Hz).

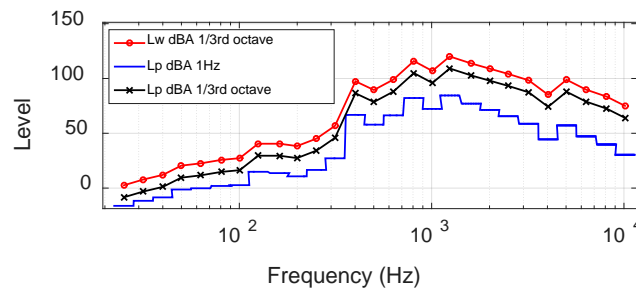


Figure 11. A-weighted sound power level (L_w), SPL (L_p dBA 1/3rd octave) equivalent spectra of a typical siren [40] at 1/3rd octave frequency band and 1 Hz resolution band (L_p dBA 1 Hz).

- Obtaining the pressure attenuation $A(f)$ in dB as a function of frequency using the *PARDOS* software tool with the barrier cap configuration presenting the highest IL. Then, an interpolation of the different frequencies of the source is carried out.
- Subtraction of the obtained attenuation (A):

$$L_p(\text{dB(A)})_{rx, 1\text{Hz}} = L_p(\text{dB(A)})_{tx, 1\text{Hz}} - A(f) \tag{31}$$

- Calculation of the global final SPL for the whole frequency range (n frequency bins):

$$L_{pA, Total, rx} = 10 \cdot \log_{10} \left(\sum_{n=1}^N 10^{\frac{L_{p,n}(\text{dB(A)})_{rx, 1\text{Hz}}}{10}} \right) \tag{32}$$

Assumption about the total SPL at the receiver exceeding the background noise must be met.

3. Results and Discussion

First, a comparison of the *IL* performance of the different single-cap barriers along the whole frequency band (from 100 Hz to 10 kHz) was carried out. Figures 12–15 illustrate the results recorded for the four configurations under analysis (i.e., ‘Car–Person’, ‘Car–Balcony’, ‘Ambulance–Person’, ‘Ambulance–Balcony’, respectively). The curves for a single screen barrier without any cap are also shown as a reference.

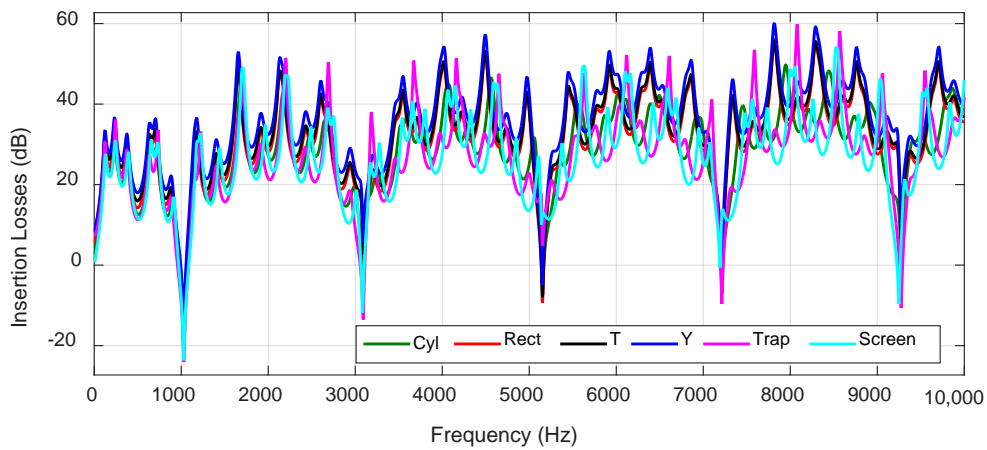


Figure 12. *IL* in Configuration 1 ‘Car–Person’ for single caps and a single screen barrier as a reference.

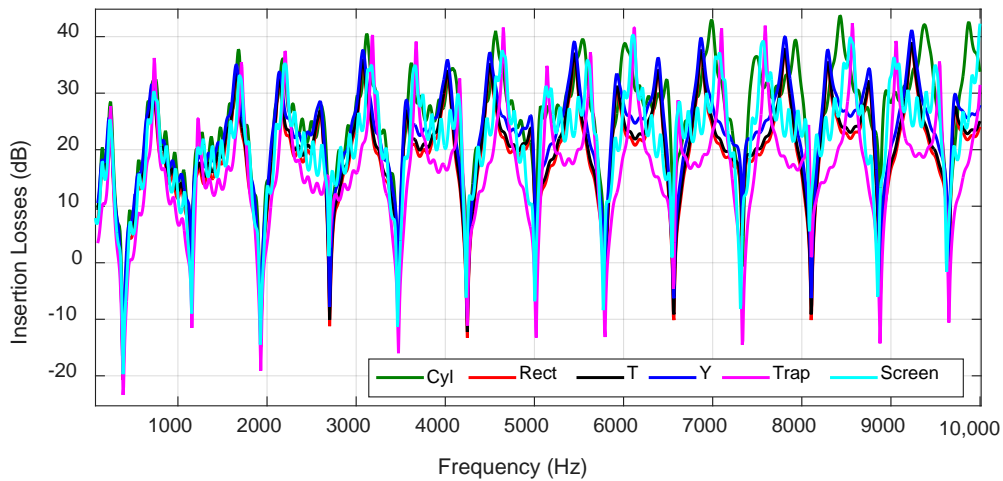


Figure 13. *IL* in Configuration 2 ‘Car–Balcony’ for single caps and a single screen barrier as a reference.

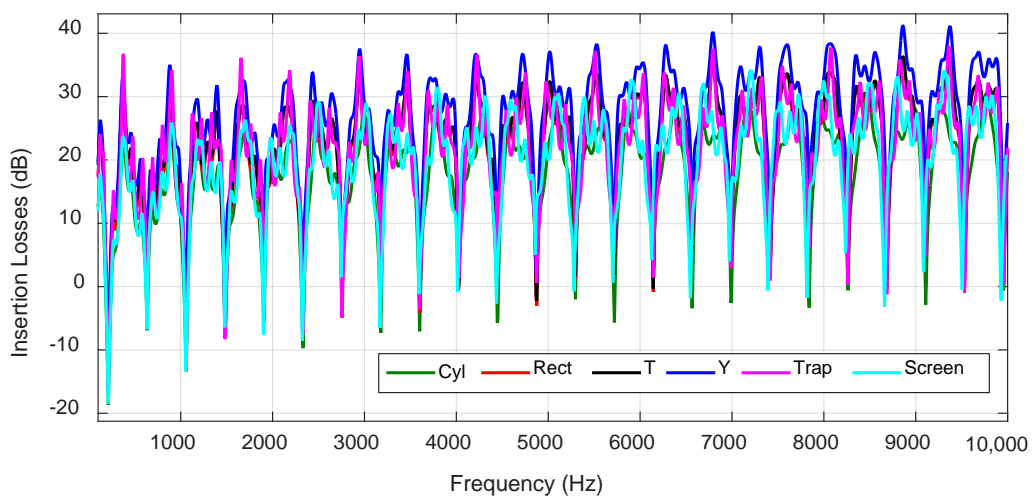


Figure 14. *IL* in Configuration 3 ‘Ambulance–Person’ for single caps and a single screen barrier as a reference.

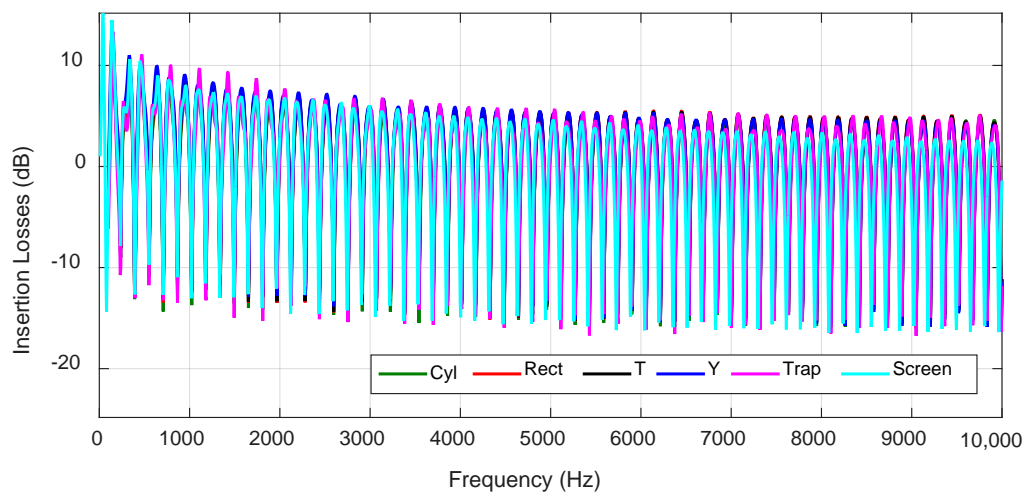


Figure 15. *IL* in Configuration 4 ‘Ambulance–Balcony’ for single caps and a single screen barrier as a reference.

As can be observed, the *IL* results for single caps revealed similar behavior as a function of frequency in all cases, with maximum *IL* values sitting at approximately 40 dB in ‘Car–Balcony’ and ‘Ambulance–Person’ configurations and up to 60 dB in the ‘Car–Person’ configuration. However, the Y-shaped cap showed slightly better performance (higher *IL*) in ‘Car–Person’ and ‘Ambulance–Person’ configurations and the cylindrical single cap showed better performance in the ‘Car–Balcony’ configuration. However, as expected, significantly lower performance for all cap types was recorded in the ‘Ambulance–Balcony’ configuration. This is because the transmitter and the receiver were less immersed in the shadow zone in this configuration (that is, a LoS between the source and the receiver exists.).

The presence of clear repetitive patterns can be instantly discerned from Figures 12–15 with insertion losses periodically falling even below 0 dB. Specifically, for Figure 12, the insertion loss drop occurred every 2054 hertz, while in Figure 13, every 775 hertz, or every 420 and about 155 hertz in Figures 14 and 15, respectively. This was because the direct and ground reflected path signals in the ‘free space’ had an opposite-phase at specific frequencies and interfered destructively and almost canceled each other out. As a consequence, ϕ_{fs} reached a minimum and *IL* also decreased to the lowest value following Equation (25).

Furthermore, the *IL* achieved by the 25 possible double-cap barriers in the four configurations was compared. For the sake of clarity and space, only a selected few simulation results are presented in this manuscript. However, it was observed overall that the maximum *IL* always involved at least one Y-shape cap. This may be due to the contribution of the higher number of diffracting “nodes” (three nodes) over the top of Y caps when compared with the other structures, which had fewer diffracting points; moreover, the result was sensitive to the specific position of the caps. Given these observations, the most representative *IL* results when double caps were used including Y-shaped caps are illustrated in Figures 16–19. The *IL* of a single screen barrier of 3 m height, without caps, for the same configuration of source and receiver, was also included in the plot as a reference.

First, as expected, an increase in *IL* could be seen across the whole frequency range when double caps were used in comparison to when single caps were applied despite the same global envelope being maintained. A careful analysis of the results led to the conclusion that the best cap configuration in terms of maximizing *IL* was a Y-shaped double cap, which, in general, offered the highest *IL* both across the whole frequency range and in the four configurations considered excluding the cylindrical Y-shaped double cap, the performance of which is slightly more elevated than that of the Y-shaped double cap in the ‘Car–Balcony’ configuration only.

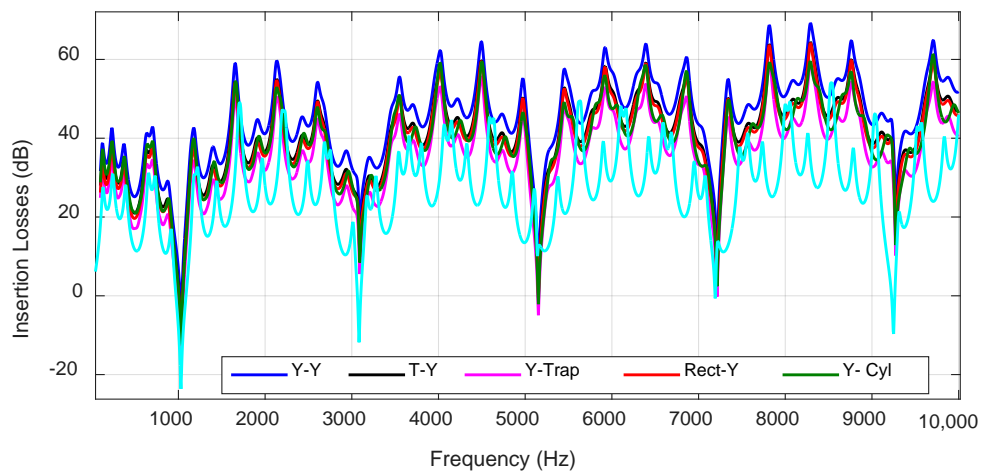


Figure 16. *IL* for Configuration 1 ('Car–Person') considering double caps formed with Y-shaped structures and a single screen barrier as a reference.

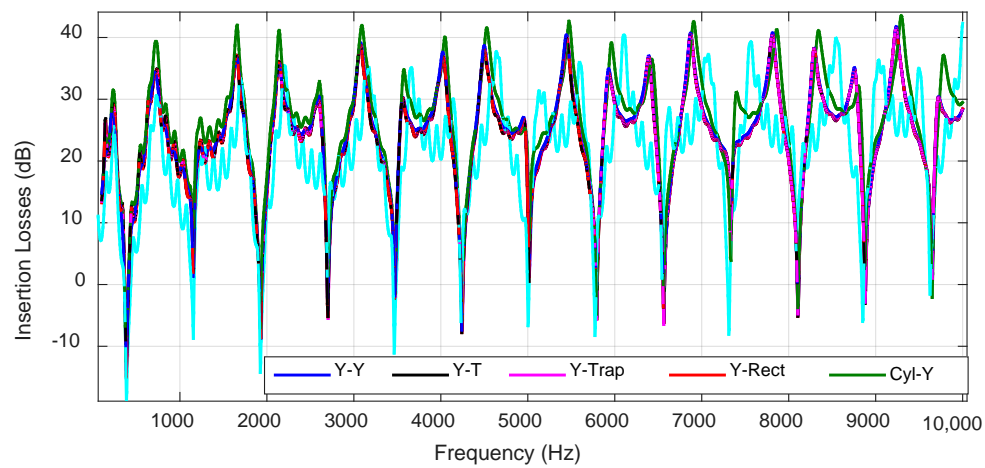


Figure 17. *IL* in Configuration 2 ('Car–Balcony') using double caps formed with Y-shaped structures and a single screen barrier as a reference.

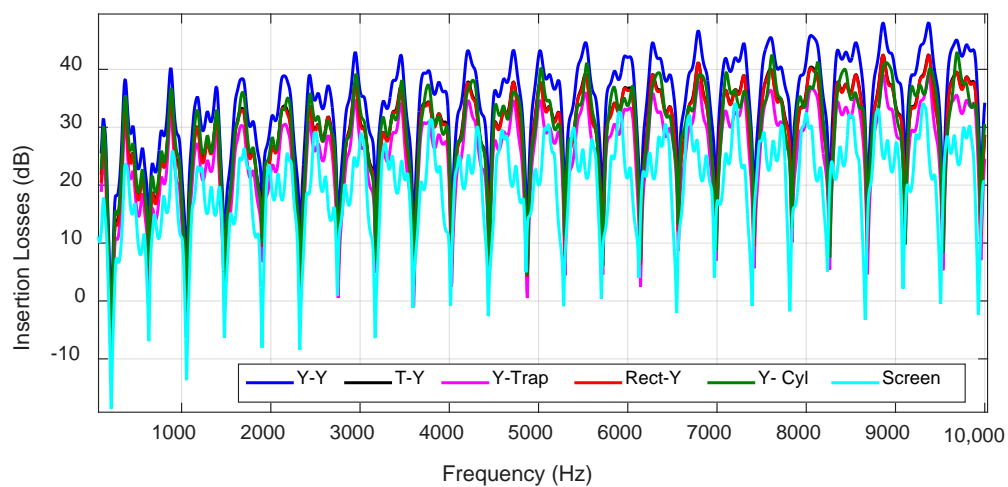


Figure 18. *IL* in Configuration 3 ('Ambulance–Person') using double caps formed with Y-shaped structures and a single screen barrier as a reference.

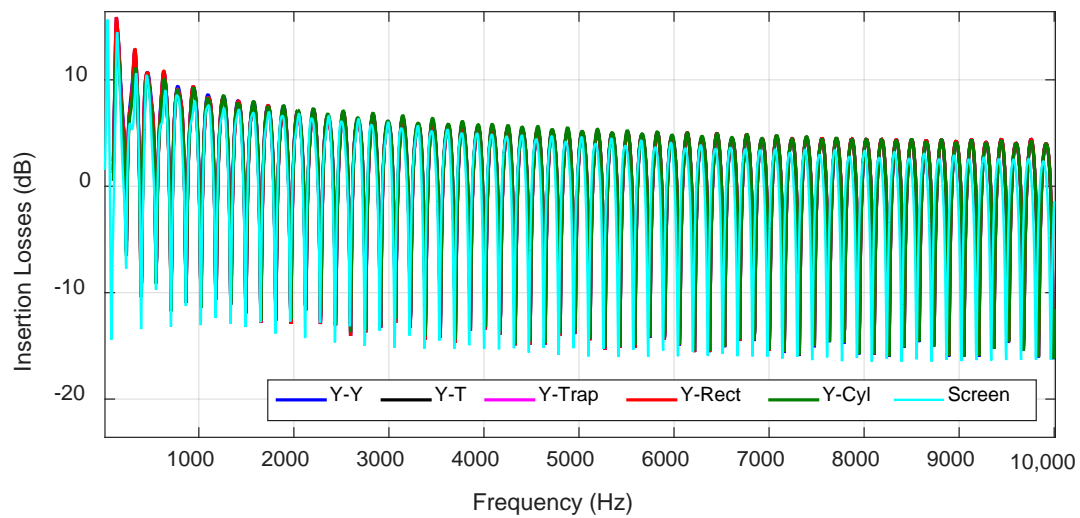


Figure 19. *IL* in Configuration 4 (‘Ambulance–Balcony’) using double caps formed with Y-shaped structures and a single screen barrier as a reference.

Nonetheless, in the ‘Ambulance–Balcony’ configuration, again as expected, the *IL* performance was lower when compared with the other three configurations. This is because a LoS exists between the receivers (potential listeners) and the source of noise. Moreover, in this configuration, the selection of the cap type did not seem to be a key issue in the final *IL* obtained.

Again, a similar behavior was verified in the evolution of the insertion losses as was found in the configurations with a single cap. This was for the same reason discussed above, and is highlighted in Figure 20 where the correlation between *IL* for the optimum double Y caps and attenuation in free space is evidenced.

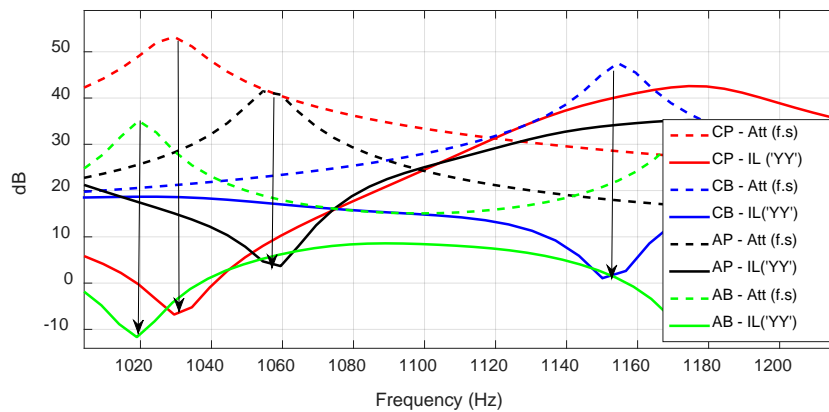


Figure 20. *IL* (solid lines) with double-Y caps in the four configurations (CP, Car–Person; CB, Car–Balcony; AP, Ambulance–Person; AB, Ambulance–Balcony) and attenuation losses (dashed lines) in free space (‘Att (fs)’, without barrier) in the corresponding receiver locations.

It can be clearly seen that the frequencies where the maximum attenuation values in free space take place coincide with the minimum levels of insertion loss ($IL \propto \phi_{fs} \propto 1/Att_{fs}$). The arrows in the graph highlight how *IL* and attenuation in ‘free space’ are inversely proportional.

Finally, both the *IL* and sound attenuation maps are displayed at 1500 Hz for the optimum cap combination (double Y cap) in Figures 21–24.

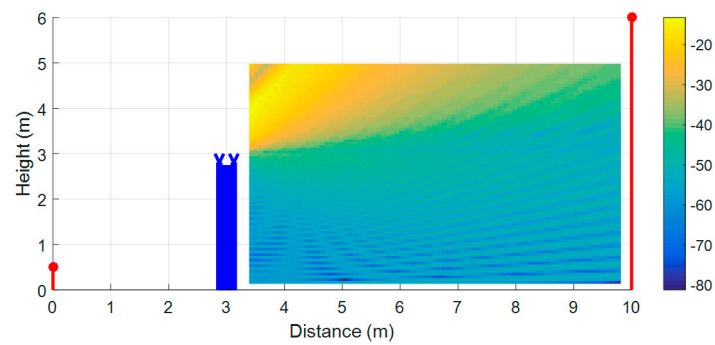


Figure 21. Attenuation map at 1500 Hz in the 'car' location. Barrier with the 'Y-Y' cap and 3 m height.

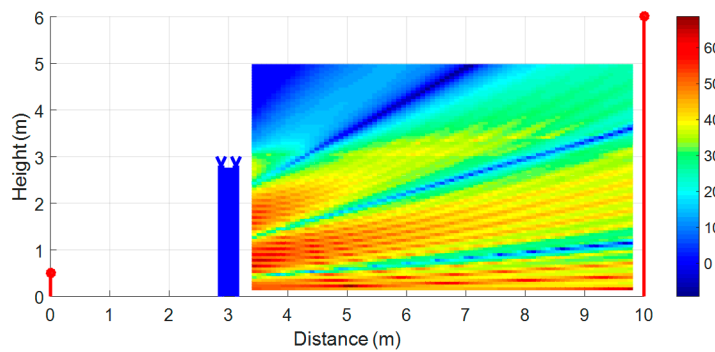


Figure 22. IL map at 1500 Hz in the 'car' location. Barrier with the 'Y-Y' cap and 3 m height.

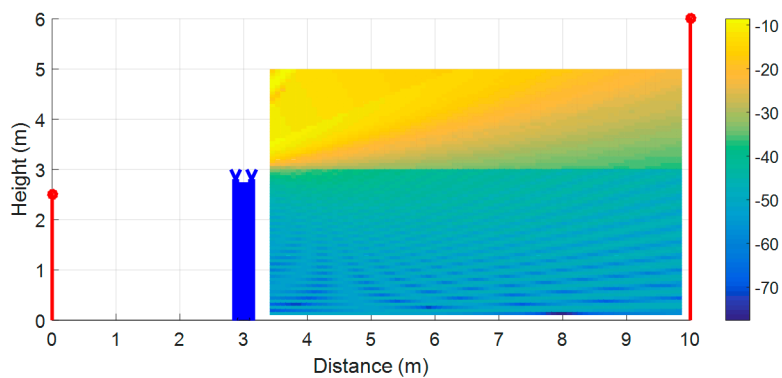


Figure 23. Attenuation map at 1500 Hz at the 'ambulance' location. Barrier with the 'Y-Y' cap and 3 m height.

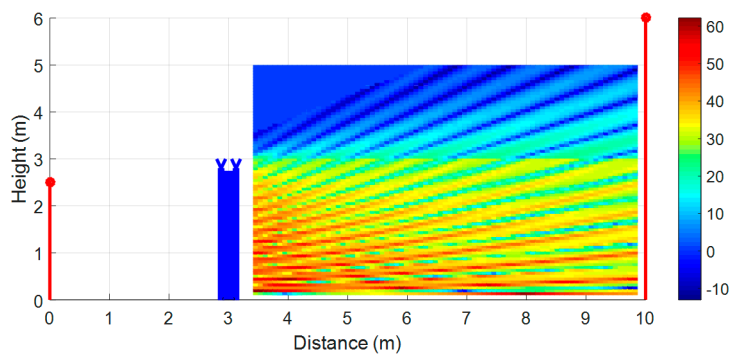


Figure 24. IL map at 1500 Hz at the 'ambulance' location. Barrier with 'the Y-Y' cap and 3 m height.

The following figures show the A-weighted sound pressure spectrum level in each 1 Hz band at the receiving positions for the selected Y-shaped double cap (including the ground reflection). Specifically, Figures 25 and 26 show the car scenarios ('Car–Person' and 'Car–Balcony' configurations, respectively) and Figures 24 and 25 illustrate the results for the ambulance scenarios ('Ambulance–Person' and 'Ambulance–Balcony' configurations, respectively). These results were compared with those recorded for scenarios where conventional screen barriers (without caps) and Y-shaped double caps were used without considering the ground reflection on the barrier source side.

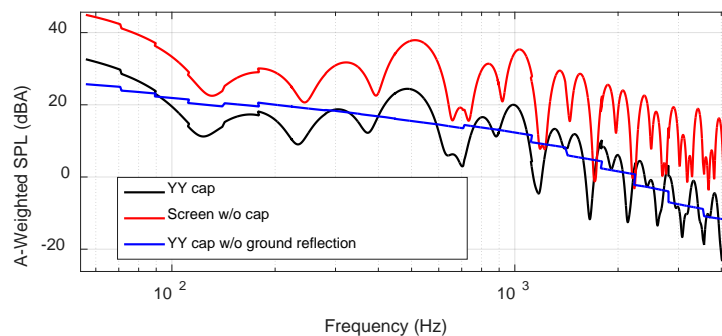


Figure 25. A-weighted SPL spectrum with 1 Hz resolution in Configuration 1 (Car–Person) for 'YY' cap with and without ground reflection. The screen barrier SPL spectrum is shown as a reference.

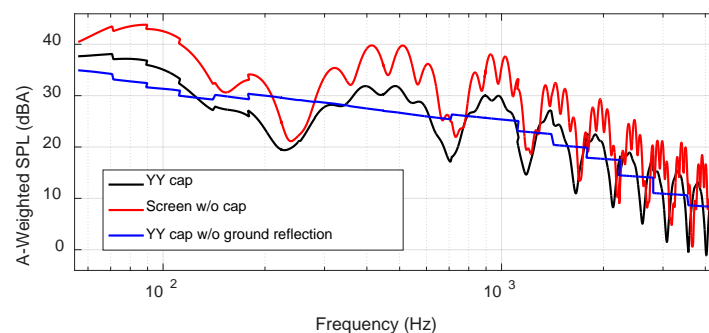


Figure 26. A-weighted sound pressure level (SPL) spectrum in 1 Hz bands in Configuration 2 (Car–Balcony) for the 'YY' cap with and without ground reflection. The screen barrier SPL spectrum is shown as a reference.

As can be observed in Figure 25, the SPL spectrum was significantly lower across the whole frequency range under analysis in the 'Car–Person' configuration when a Y-shaped double cap was added to the barrier compared to when plain screen barriers without caps were used in the same scenario. When a comparison was made under the conditions of the 'Car–Balcony' configuration (Figure 26) between the use of Y-shaped double caps and a single screen, the improvement in terms of *IL* when Y-shaped double caps were used is clear, although not as significant as in the 'Car–Person' configuration. Finally, the impact of canceling out the ground reflection on the SPL is that fluctuations in SPL are removed throughout the whole frequency band.

Similarly, as can be observed in Figure 27, again, the highest SPL reduction in the 'Ambulance–Person' configuration as achieved when the Y-shaped double cap was used (with ground reflection). However, this was not that clear from the results recorded for the 'Ambulance–Balcony' configuration (Figure 28) since, as mentioned before, a LoS exists in this case and the influence of the modeling of the caps thus has less of an impact. Once more, the removal of the ground reflection leads to smoothed curves in the pressure levels, but with a similar evolution with respect to the cases with reflections.

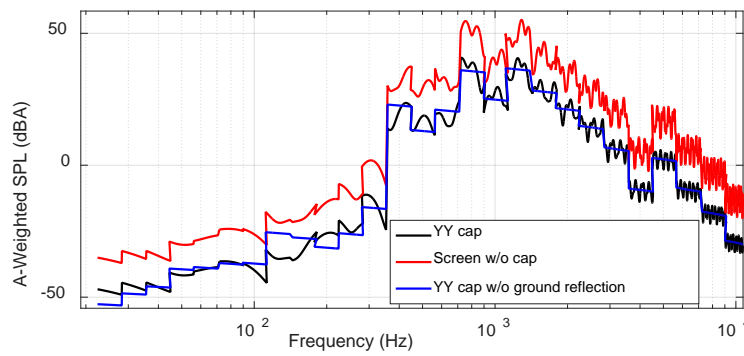


Figure 27. A-weighted SPL spectrum in 1 Hz bands in Configuration 3 (Ambulance–Person) for the ‘YY’ cap with and without ground reflection. The screen barrier SPL spectrum is shown as a reference.

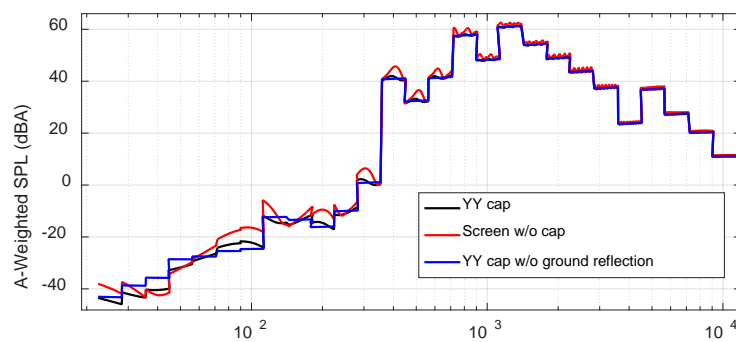


Figure 28. A-weighted SPL spectrum in 1 Hz bands in Configuration 4 (Ambulance–Balcony) for ‘YY’ cap with and without ground reflection. The screen barrier SPL spectrum is shown as a reference.

Finally, following Equation (32), the global A-weighted sound pressure spectrum levels (considering the whole frequency band) at the receiver locations (LdBARx) were numerically estimated, presented, and compared (Table 1) across the following scenarios: in the absence of a noise barrier; in the presence of a plain screen without a cap; in the presence of a plain screen with Y-shaped double caps; and in the presence of a plain screen with Y-shaped double caps without ground reflection at the source side of the barrier.

Table 1. Global sound pressure level (SPL) (dBA) at receiver positions.

Scenario	‘Car’ (Road Traffic) Lw (dBA) = 110.2 Lp(dBA) = 99.2		‘Ambulance’ (Ambulance Siren) Lw (dBA) = 122.6 Lp(dBA) = 111.6	
	LdBARx ‘Person’ Conf 1	LdBARx ‘Balcony’ Conf 2	LdBARx ‘Person’ Conf 3	LdBARx ‘Balcony’ Conf 4
Free path, without barrier	87.8	85.1	99.5	97.9
Plain screen barrier without caps	63.7	66.7	78.6	89.2
Y-shaped double cap on top of barrier	50.0	60.4	64.6	88.2
Y-shaped double cap on top of barrier w/o ground reflection	47.7	58.9	63.6	88.2

As can be seen in Table 1, the global A-weighted SPL for road traffic in the ‘Car–Person’ configuration when Y-shaped double caps were used was within the safe levels with an equivalent SPL well below the threshold of 55 dB(A), which is considered by the WHO to be the level at which “serious annoyance, daytime and evening, for outdoor living areas” occur. Furthermore, there was an additional attenuation of about 14 dB in the ‘Car–Person’ and ‘Ambulance–Person’ configurations and 6 dB in the ‘Car–Balcony’ configuration when compared with plain screen barriers without caps

(for the ‘Ambulance–Balcony’ configuration, it has previously been verified that the modeling of the top barrier is not a relevant consideration). The performance of the barriers can also be enhanced (by 2.3 dB and 1.5 dB for person and balcony cases, respectively) if the ground is absorbing and the reflection from the side of the source can be discarded. Additionally, when the source is a vehicle siren (ambulance), the Y-shaped double cap improves the performance of conventional plain screen barriers by about 14 dB in the case of a person at street level as a receiver, and by a further 1 dB if the ground reflection is properly absorbed. However, again, the improvement in terms of IL seems to be largely negligible when caps are attached to the top of conventional screen barriers where a LoS exists between the source and the receiver (‘Ambulance–Balcony’ case) with just 1 dB of additional attenuation and even less if the reflection on the ground is canceled out.

It should be noted that canceling out the ground reflection on the listener side of the barrier and its impact on IL was also analyzed, but the simulations revealed only a negligible impact on final SPL since the IL was quite similar to scenarios where the ground reflection at this side was present.

3.1. Influence of Sloping Ground on Global Acoustic Insertion Losses

As can be seen in Table 2, when the ground was angled to a certain degree (in this instance 5° or 10°) and a Y-shaped double cap was attached to the top of a conventional barrier (Figure 29), the global SPL at the receiving point decreased for person-like receivers (‘Car–Person’ and ‘Ambulance–Person’ configurations) as compared with a flat road scenario. However, there is no clear improvement (‘Ambulance–Balcony’) or the result is even slightly worse (‘Car–Balcony’) for “balcony” receivers when compared with the SPL obtained in the scenario involving a flat road and Y-shaped double caps. This could be explained by the fact that the height of the barrier increased with the ground positive slope ($\Delta H_{\text{bar}} = d_1 \cdot \tan(\alpha)$), thereby leading to ‘Person’ locations to be more deeply immersed in the shadow region (despite also being elevated due to the sloping ground by $\Delta H = (d_1 + d_2) \cdot \tan(\alpha)$).

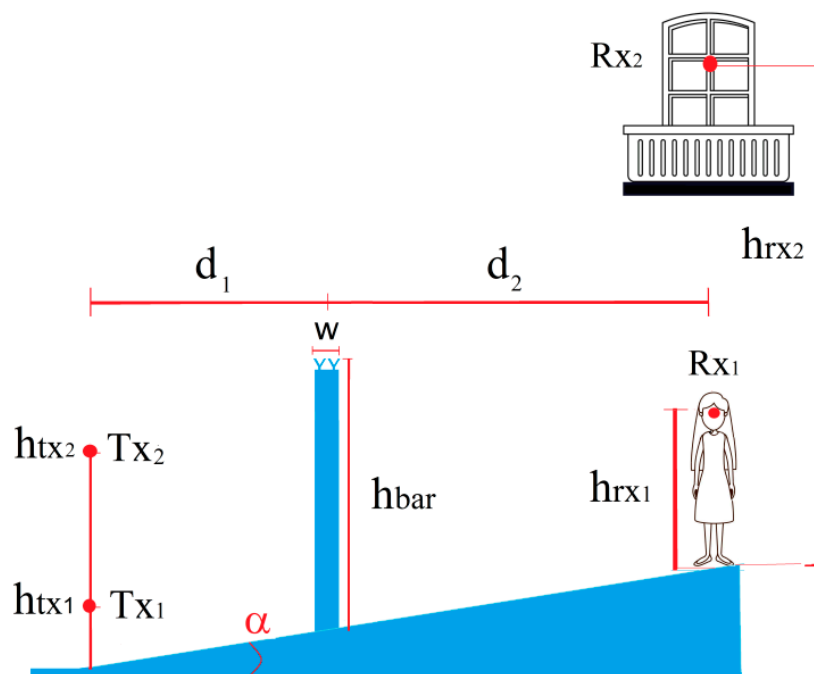


Figure 29. All configurations with a road slope at angle α .

Table 2. Global SPL (dBA) at the receiver positions for Y-shaped double cap and sloping ground.

Scenario	'Car' (Road Traffic) Lw (dBA) = 110.2 Lp(dBA) = 99.2		'Ambulance' (Ambulance Siren) Lw (dBA) = 122.6 Lp(dBA) = 111.6	
	LdBArx 'Person' Conf 1	LdBArx 'Balcony' Conf 2	LdBArx 'Person' Conf 3	LdBArx 'Balcony' Conf 4
Y-shaped double cap with ground slope angle of 5°	45.7	61.1	59.8	87.8
Y-shaped double cap with ground slope angle of 5° and w/o ground reflection	42.7	59.7	58.1	87.8
Y-shaped double cap with ground slope angle of 10°	46.3	61.4	60.7	87.4
Y-shaped double cap with ground slope angle of 10° and w/o ground reflection	43.1	59.9	58.8	87.4

The simultaneous use of both techniques (sloping and absorbing grounds), together with double Y caps on the top of barriers, led to the most promising results for the 'Person' listener configuration, with an additional global SPL mitigation of about 6–7 dB when compared with scenarios with flat and reflecting grounds and double Y caps. Figure 30 shows the SPL comparison for the 'Car–Person' configuration, where the improvement was confirmed. It is also important to note that the performances for the configurations with 'Balcony' listeners in the presence of sloping or absorbent grounds did not worsen, but were similar to the results obtained in the absence of both strategies.

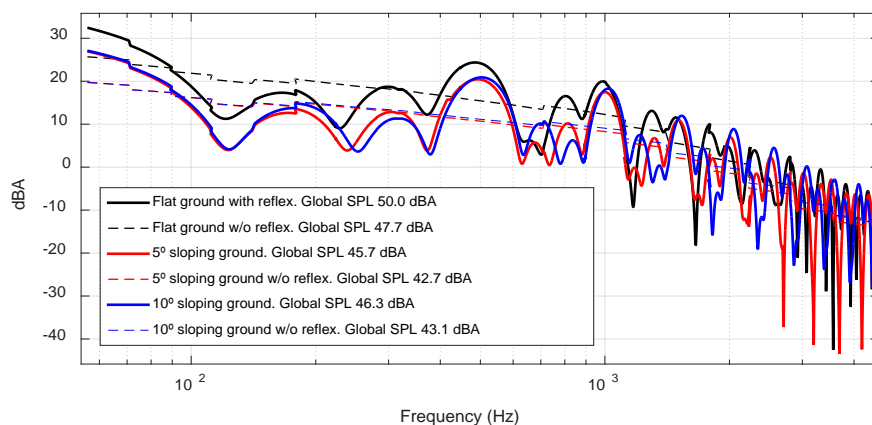


Figure 30. Influence of sloping and reflecting grounds on the SPL spectrum for the 'Car–Person' configuration and barrier with optimum double Y caps.

3.2. Influence of Increasing the Number of Diffracting Devices (More than Two) while Maintaining the Same Envelope Size

As can be seen in Table 3, this study also verified that, when the number of diffracting elements is progressively increased (from two caps) while the maximum envelope size is maintained (Figure 31), IL does not rise accordingly in all cases as seen when Y-shaped double caps are used. Rather, and contrary to what might be expected, SPLs for Y-shaped triple caps performed less effectively than Y-shaped double caps (except in the 'Car–Balcony' configuration). This finding is consistent with the fact that, below a certain size, the diffracting object can start to lose its effectiveness over certain frequency bands.

Table 3. Global SPL (dBA) at the receiver positions for Y-shaped triple caps.

Scenario	'Car' (Road Traffic) Lw (dBA) = 110.2 Lp(dBA) = 99.2		'Ambulance' (Ambulance Siren) Lw (dBA) = 122.6 Lp(dBA) = 111.6	
	LdBArx 'Person' Conf 1	LdBArx 'Balcony' Conf 2	LdBArx 'Person' Conf 3	LdBArx 'Balcony' Conf 4
Y-shaped triple cap on top of barrier with ground reflection	53.4	52.9	67.2	87.8

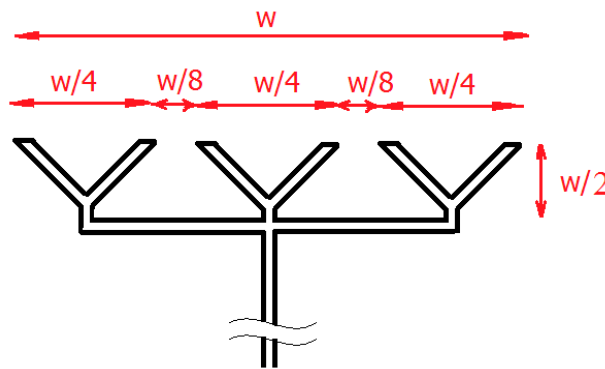


Figure 31. Triple Y-cap.

4. Conclusions

In this work, the performance of acoustic noise barriers when additional structures (cap elements) of different types were attached to the top of conventional screen barriers was analyzed for a broad frequency band (from 100 Hz up to 10 kHz).

Various configurations were tested, with two transmitters (a “Car” source at a height of 0.5 m and an “Ambulance” source at a height of 2.5 m), two receivers (a “Person” location at a height of 1.7 m and a “Balcony” listener at a height of 5 m), and five different cap shapes (“Y-shaped,” “T-shaped,” “rectangle,” “cylinder,” and “trapezoid,” along with double combinations). Caps were attached to the top of 3 m high conventional, plain barriers.

Exhaustive analyses revealed that caps improved noise mitigation when compared with conventional plain barriers of the same height not only for traffic road noise, but also for vehicle siren sounds. Specifically, the results revealed that optimal performance was achieved when Y-shaped double caps were used, with an additional noise abatement of about 14 dB being achieved in the “Car–Person” and “Ambulance–Person” configurations and slightly more than 6 dB in the “Car–Balcony” configuration as compared with the use of conventional screens.

Furthermore, the analysis of the ground reflection on the source side revealed that its removal by absorbing materials could also provide a meaningful additional improvement in terms of *IL*, and SPLs can accordingly be diminished by about 2.5 dB in the “Car–Person” and “Car–Balcony” configurations and 1 dB in the “Ambulance–Person” configuration, as shown in Table 1. The simultaneous use of both techniques (sloping and absorbing grounds), together with double Y caps on top of barriers, led to the most promising results for the “Person” listener configuration, with an additional global SPL mitigation of about 6–7 dB when compared with scenarios with flat and reflecting grounds and double Y-shaped caps.

This study also verified that it is not worthwhile to indefinitely increase the number of diffraction elements (e.g., the use of Y-shaped triple caps) while maintaining the global envelope size of the barrier since the SPL is higher in these instances than in other, simpler settings (e.g., the use of Y-shaped double caps). In contrast, the consideration of the slope of the road can lead to an increase in noise isolation, especially when the receivers are located at lower heights (“Person” listener).

The authors intend to focus their future research on reviewing, extending, and validating the present work by considering other diffracting structures (e.g., branched caps) and performing the corresponding measurement analyses. The impact of absorbing materials on the surfaces of the cap elements on noise abatement will also be analyzed.

Author Contributions: Conceptualization, D.P.-Q. and J.-V.R.; Methodology, D.P.-Q.; Software, D.P.-Q.; Validation, D.P.-Q.; Formal analysis, D.P.-Q.; Investigation, D.P.-Q. and J.-V.R.; Resources, D.P.-Q., J.-V.R., J.-M.M.G.-P., and L.J.-L.; Data curation, D.P.-Q.; Writing—original draft preparation, D.P.-Q.; Writing—review and editing, D.P.-Q., J.-V.R., J.-M.M.G.-P., and L.J.-L.; Visualization, D.P.-Q., J.-V.R., J.-M.M.G.-P., and L.J.-L.; Supervision, J.V.R.; Project administration, J.-M.M.G.-P., and L.J.-L.; Funding acquisition, J.-M.M.G.-P., and L.J.-L. All authors have read and agreed to the published version of the manuscript.

Funding: This work was funded by the Ministerio de Ciencia e Innovación, Spain (TEC2016-78028-C3-2-P and PID2019-107885GB-C33), and by the European Fonds Européen de Développement Économique et Régional (FEDER) funds.

Conflicts of Interest: The authors declare no conflict of interest. The funders had no role in the design of the study; in the collection, analyses, or interpretation of data; in the writing of the manuscript; or in the decision to publish the results.

References

- Berglund, B.; Lindvall, T.; Schwela, D.H. (Eds.) *Guidelines for Community Noise*; World Health Organization: Geneva, Switzerland, 1999; Available online: <http://whqlibdoc.who.int/hq/1999/a68672.pdf> (accessed on 22 July 2010).
- JRC European Commission. *Burden of Disease from Environmental Noise. Quantification of Healthy Life Years Lost in Europe*; World Health Organization: Copenhagen, Denmark, 2011; ISBN 978 92 890 0229 5.
- Fredianelli, L.; Carpita, S.; Licitra, G. A procedure for deriving wind turbine noise limits by taking into account annoyance. *Sci. Total. Environ.* **2019**, *648*, 728–736. [[CrossRef](#)] [[PubMed](#)]
- Basner, M.; Babisch, W.; Davis, A.; Brink, M.; Clark, C.; Janssen, S.; Stansfeld, S. Auditory and non-auditory effects of noise on health. *Lancet* **2014**, *383*, 1325–1332. [[CrossRef](#)]
- Sygná, K.; Aasvang, G.M.; Aamodt, G.; Oftedal, B.; Krogh, N.H. Road traffic noise, sleep and mental health. *Environ. Res.* **2014**, *131*, 17–24. [[CrossRef](#)]
- Licitra, G.; Fredianelli, L.; Petri, D.; Vigotti, M.A. Annoyance evaluation due to overall railway noise and vibration in Pisa urban areas. *Sci. Total. Environ.* **2016**, *568*, 1315–1325. [[CrossRef](#)]
- Lercher, P.; Evans, G.W.; Meis, M. Ambient noise and cognitive processes among primary schoolchildren. *Environ. Behav.* **2003**, *35*, 725–735. [[CrossRef](#)]
- Chetoni, M.; Fredianelli, L.; Minichilli, F.; Cori, L.; Licitra, G.; Bianco, F. Correlation between perceived and measured noise, within the Gioconda project. In Proceedings of the ICSV 2016–23rd International Congress on Sound and Vibration: From Ancient to Modern Acoustics, Athens, Greece, 10–14 July 2016.
- Vienneau, D.; Schindler, C.; Perez, L.; Probst-Hensch, N.; Rösli, M. Hypertension ischemic heart disease. The relationship between transportation noise exposure and ischemic heart disease: A meta-analysis. *Environ. Res.* **2015**, *138*, 372–380. [[CrossRef](#)]
- Roswall, N.; Raaschou-Nielsen, O.; Ketzler, M.; Gammelmark, A.; Overvad, K.; Olsen, A.; Sørensen, M. Long-term residential road traffic noise and NO₂ exposure in relation to risk of incident myocardial infarction—A Danish cohort study. *Environ. Res.* **2017**, *156*, 80–86. [[CrossRef](#)]
- Roswall, N.; Raaschou-Nielsen, O.; Jensen, S.S.; Tjønneland, A.; Sørensen, M. Long-term exposure to residential railway and road traffic noise and risk for diabetes in a Danish cohort. *Environ. Res.* **2018**, *160*, 292–297. [[CrossRef](#)]
- Śliwińska-Kowalska, M.; Zaborowski, K. WHO Environmental Noise Guidelines for the European Region: A Systematic Review on Environmental Noise and Permanent Hearing Loss and Tinnitus. *Int. J. Environ. Res. Public Health* **2017**, *14*, 1139. [[CrossRef](#)]
- Del Pizzo, A.; Luca, T.; Moro, A.; Bianco, F.; Fredianelli, L. Influence of texture on tyre road noise spectra in rubberized pavements. *Appl. Acoust.* **2020**, *159*, 107080. [[CrossRef](#)]
- Teti, L.; De León, G.; Del Pizzo, A.; Moro, A.; Bianco, F.; Fredianelli, L.; Licitra, G. Modelling the acoustic performance of newly laid low-noise pavements. *Constr. Build. Mater.* **2020**, *247*, 118509. [[CrossRef](#)]

15. Praticò, F.G.; Moro, A. Permeability and volumetrics of porous asphalt concrete: A theoretical and experimental investigation. *Road Mater. Pavement Des.* **2007**, *8*, 799–817. [[CrossRef](#)]
16. Praticò, F.G. Roads and loudness: A more comprehensive approach. *Road Mater. Pavement Des.* **2001**, *2*, 359–377. [[CrossRef](#)]
17. Licitra, G.; Cerchiai, M.; Teti, L.; Ascari, E.; Bianco, F.; Cheton, M. Performance assessment of low-noise road surfaces in the Leopoldo project: Comparison and validation of different measurement methods. *Coatings* **2015**, *5*, 3–25. [[CrossRef](#)]
18. Fredianelli, L.; Del Pizzo, A.; Licitra, G. Recent developments in sonic crystals as barriers for road traffic noise mitigation. *Environments* **2019**, *6*, 14. [[CrossRef](#)]
19. Radosz, J. Acoustic performance of noise barrier based on sonic crystals with resonant elements. *Appl. Acoust.* **2019**, *155*, 492–499. [[CrossRef](#)]
20. Godinho, L.; Redondo, J.; Amado-Mendes, P. The method of fundamental solutions for the analysis of infinite 3D sonic crystals. *Eng. Anal. Bound. Elem.* **2019**, *98*, 172–183. [[CrossRef](#)]
21. Watts, G.R. Acoustic performance of new designs of traffic noise barriers: Full-scale tests. *J. Sound Vib.* **1994**, *177*, 289–305. [[CrossRef](#)]
22. Watts, G.R. Acoustic performance of a multiple-edge noise barrier profile at motorway sites. *Appl. Acoust.* **1996**, *47*, 47–66. [[CrossRef](#)]
23. Watts, G.R.; Morgan, P.A. Acoustic performance of an interference type noise barrier. *Appl. Acoust.* **1964**, *49*, 1–16. [[CrossRef](#)]
24. Watts, G.R. Effectiveness of novel shaped bunds in reducing traffic noise. *Proc. Inst. Acoust.* **1999**, *21*, 41–50.
25. Haan, C.; Kim, S. Comparison of the insertion loss of noise barriers with different shapes of upper structure. In Proceedings of the Road Traffic Noise Modeling and Noise Barrier, 22nd International Congress on Acoustics, ICA, Buenos Aires, Argentina, 5–9 September 2016.
26. Ishizuka, T.; Fujiwara, K. Performance of noise barriers with various edge shapes and acoustical conditions. *Appl. Acoust.* **2004**, *65*, 125–141. [[CrossRef](#)]
27. Asdrubali, F. On the experimental evaluation of the performances of noise barrier diffracting devices. *Acta Acust. United Acust.* **2007**, *93*, 659–669.
28. Monazzam, M.; Fard, S. Performance of passive and reactive profiled median barriers in traffic noise reduction. *J. Zhejiang Univ. Sci. A Appl. Phys. Eng.* **2011**, *12*, 78–86. [[CrossRef](#)]
29. Yamamoto, K. Japanese experience to reduce road traffic noise by barriers with noise-reducing devices. In Proceedings of the 10th European Congress and Exposition on Noise Control Engineering, EuroNoise, Maastricht, The Netherlands, 31 May–3 June 2015; Volume 31.
30. Monazzam, M.; Abbasi, M.; Yazdanirad, S. Performance Evaluation of T-Shaped Noise Barriers Covered with Oblique Diffusers Using Boundary Element Method. *Arch. Acoust.* **2019**, *44*, 521–531. [[CrossRef](#)]
31. Morgan, P. *QUESTIM. Assessing the Acoustic Durability of Noise Barriers on NRA Road Networks*; CEDR Transnational Road Research Programme; CEDR: London, UK, 2014.
32. Vanhooreweder, B.; Marcocci, S.; De Leo, A. *State of the Art in Managing Road Traffic Noise: Noise Barriers*; Technical Report 2017-02; CEDR: London, UK, 2016; ISBN 979-10-93321-27-1.
33. May, D.N.; Osman, M.M. The performance of sound absorptive, reflective and T-profile noise barriers in Toronto. *J. Sound Vib.* **1980**, *71*, 65–71. [[CrossRef](#)]
34. Can, A.; Leclercq, L.; Lelong, J.; Botteldooren, D. Traffic Noise Spectrum Analysis: Dynamic Modeling vs. Experimental Observations. *Appl. Acoust.* **2010**, *71*, 765–770. [[CrossRef](#)]
35. Jakovljevic, B.; Paunovic, K.; Belojevic, G. Road-Traffic Noise and Factors Influencing Noise Annoyance in an Urban Population. *Environ. Int.* **2009**, *35*, 552–556. [[CrossRef](#)]
36. Dravitzki, V.; Walton, D.K.; Wood, W.B. *Determining the Influence of New Zealand Road Surfaces on Noise Levels and Community Annoyance*; Report 292; Land Transport New Zealand: Wellington, New Zealand, 2006.
37. EN 1793-3. *Road Traffic Noise Reducing Devices—Test Method for Determining the Acoustic Performance—Part 3; Normalized Traffic Noise Spectrum*; European Committee for Standardization: Brussels, Belgium, 1997.
38. Baulac, M.; Guillou, A.; Defrance, J.; Jean, P. Calculations of low height noise barriers efficiency by using Boundary Element Method and optimization algorithms. *J. Acoust. Soc. Am.* **2008**. [[CrossRef](#)]
39. Catchpole, K.R. A framework for the design of ambulance sirens. *Ergonomics* **2007**, *50*, 1287–1301. [[CrossRef](#)]
40. Howard, C. Acoustic characteristics for effective ambulance sirens. *Aust. Acoust. Soc.* **2011**, *39*, 43–53.

41. U.S. Department of Transportation Federal Highway Administration. Available online: https://www.fhwa.dot.gov/Environment/noise/noise_barriers/inventory/summary/stable713.cfm (accessed on 18 August 2020).
42. Morgan, P. *Review of Japanese Noise Barrier Research (DWW-2004-081)*; Rijkswaterstaat Dienst Verkeer en Scheepvaart: Delft, The Netherlands, 2004.
43. Pardo-Quiles, D.; Rodríguez, J.-V. A Fast UTD-based Method for the Analysis of Multiple Acoustic Diffractions over a Series of Obstacles with Arbitrary Modeling, Height and Spacing. *Symmetry* **2020**, *12*, 1–24.
44. Keller, B. Geometrical theory of diffraction. *J. Opt. Soc. Am.* **1962**, *52*, 116–130. [[CrossRef](#)] [[PubMed](#)]
45. Kouyoumjian, R.G.; Pathak, P.H. A uniform geometrical theory of diffraction for an edge in a perfectly conducting surface. *Proc. IEEE* **1974**, *62*, 1448–1461. [[CrossRef](#)]
46. Pierce, A.D. Diffraction of sound around corners and over wide barriers. *J. Acoust. Soc. Am.* **1974**, *55*, 941–955. [[CrossRef](#)]
47. Min, H.; Qiu, X. Multiple acoustic diffraction around rigid parallel wide barriers. *J. Acoust. Soc. Am.* **2009**, *126*, 179–186. [[CrossRef](#)]
48. Rasmussen, K. *Calculation Methods for the Physical Properties of Air Used in the Calibration of Microphones*; Report PL-11b; Department of Acoustic Technology, Technical University of Denmark: Lyngby, Denmark, 1997.
49. McNamara, D.A.; Pistorius, C.W.I.; Malherbe, J.A.G. *Introduction to the Uniform Geometrical Theory of Diffraction*; Artech House: Norwood, MA, USA, 1990.
50. Koutitas, G.; Tzaras, C. A UTD solution for multiple rounded surfaces. *IEEE Trans. Antennas Propag.* **2006**, *54*, 4. [[CrossRef](#)]
51. Rodríguez, J.-V.; Molina-García-Pardo, J.-M.; Juan-Llácer, L. A hybrid UTD-PO solution for multiple-cylinder diffraction analysis assuming spherical-wave incidence. *IEEE Trans. Antennas Propag.* **2008**, *56*, 3078–3081. [[CrossRef](#)]
52. Kinsler, L.E.; Frey, A.R.; Coppens, A.B.; Sanders, J.V. *Fundamentals of Acoustics*; Wiley: Hoboken, NJ, USA, 1999; ISBN 0-471-84789-5.
53. Fahy, F.; Rossing, T.D. *Foundations of Engineering Acoustics*; Elsevier Academic Press: London, UK, 2001; ISBN 0-12-247665-4.



© 2020 by the authors. Licensee MDPI, Basel, Switzerland. This article is an open access article distributed under the terms and conditions of the Creative Commons Attribution (CC BY) license (<http://creativecommons.org/licenses/by/4.0/>).